

Path-Integral Quantum Monte Carlo Techniques for Self-Assembled Quantum Dots

Matthew Harowitz, Daejin Shin, and John Shumway

*Department of Physics and Astronomy,
Arizona State University, Tempe, AZ 85287-1504, USA*

We have developed a set of path integral quantum Monte Carlo techniques for studying self-assembled quantum dots. The simulations can be run in two or three dimensions, with a variety of different effective mass models. Our most realistic simulations start from an atomistic model of dot shape, size, and composition, then compute strain-modified band offsets to use as input for the path integral algorithms. We have studied charge distributions and total energies for different numbers of electrons and holes in a variety of InGaAs/GaAs quantum dots. New techniques allow us to apply external electronic and magnetic fields. We have also gone beyond the parabolic band approximation by including an energy-dependent effective mass (in mathematical analogy to relativistic kinetic energy). Finally, we describe a path-integral method for calculating the degree to which biexcitonic correlation suppresses radiative recombination rates.

PACS numbers: 02.70.Ss; 73.21.La; 78.67.Hc

1. INTRODUCTION

Semiconductor nanostructures confine electron and hole excitations in small regions that extend from several to hundreds of nanometers. There are many reasons to develop nanostructures, such as their ability to enhance optical absorption and emission, the continuing miniaturization of digital circuitry, and the study of few-body quantum phenomenon and possible exploitation for quantum computation. For example, InAs/GaAs self-assembled quantum dots^{1,2} are small islands of InAs, about 20 nm wide by 3 nm tall, that exhibit photoluminescence (PL) from quantized states,^{3,4} including few-body states⁵⁻⁷ and possibly entangled states.^{8,9}

Modeling of the properties of electrons and holes in nanostructures is

complicated by a number of converging energy scales. Thermal energies range from less than 1 meV in the coldest experiments to 25 meV in room temperature devices. Both Coulomb energies and quantized energy splittings for typical nanostructures range from a few meV to a few tens of meV. This enables experimental study of study electronic states in many different regimes by adjusting the shape, dimensionality, and size of the confinement regions. In self-assembled dots, single particle states describe gross features, with correlation being crucial for subtle effects, such as biexciton binding.¹⁰ Additionally, the relative strength of external electric¹¹ and magnetic^{12,13} fields in nanostructures may be varied over a wide range, allowing the study of quantum states not typically observed in conventional atomic, molecular, and solid state physics.

In this paper we give an overview of a path integral technique that allows us to study quantum correlation, thermal excitation, and many other effects in nanostructures. These quantum Monte Carlo (QMC) techniques are based on Metropolis sampling, much like conventional classical simulations. The path integral formalism of quantum statistical mechanics¹⁴ allows fully quantum behavior to be incorporated directly into the simulation. The path integral QMC techniques have two decades of success in quantum simulations of liquid helium,¹⁵ but have required some new developments to be broadly applicable to semiconductor nanostructures.

The ground state limit of path integral QMC, diffusion QMC, is a simpler technique that has been more widely used for quantum dots.^{10,16–22} To be efficient, diffusion QMC requires an accurate trial wavefunction, from which the algorithm projects the true ground state energy. In contrast, the path integral QMC approach does not require a trial wavefunction; instead the energy, charge density density, and many other properties are sampled directly from the confining potential and other interactions. Because of the complexity of the path integral algorithm and the need for new technical developments, the path integral QMC technique has not been widely used for dots. The purpose of this paper is to summarize some of our recent advances in the path-integral QMC simulation of dots, and suggest areas for future work. Relevant open-source simulation code and other dot-modeling tools are available on our web site.²³

2. MODELING SELF-ASSEMBLED EPITAXIAL DOTS

The formation of epitaxially grown self-assembled quantum dots is strain-driven. The most commonly studied system is InAs/GaAs, due to its strong photoluminescence, but dots may be grown in many other material systems.

Growth starts on a GaAs 100 substrate. When InAs is deposited, it initially forms a thin quantum well, known as a wetting layer. The film is highly strained due to the 7% lattice mismatch between bulk InAs and bulk GaAs. To relieve strain, the InAs forms shallow islands, a process known as Stranski-Kraskinow growth.^{24–26} By depositing a GaAs capping layer over the InAs island layer, an ensemble of buried, coherently-strained InAs islands can be created.²⁶ The islands often incorporate Ga in their structure, and the exact size, shape, placement, and composition profile must be measured from experiments.²⁷

In our models, we assume that the conduction electrons and valence-band holes can be described by a single-band effective mass model. The Hamiltonian is

$$H = \sum_{i=1}^{N_e} \frac{p_i^2}{2m_e^*} + \sum_{i=1}^{N_h} \frac{p_i^2}{2m_h^*} + \sum_{i=1}^{N_e} V_e(\mathbf{r}_i) + \sum_{i=1}^{N_h} V_h(\mathbf{r}_i) + \sum_{i<j} \frac{q_i q_j}{\epsilon r_{ij}}, \quad (1)$$

where N_e and N_h are the numbers of electrons and holes, m_e^* and m_h^* are their respective effective masses, $q = \pm 1$ are the particle charges, and ϵ is the dielectric constant of the material. The confining potentials V_e for electrons and V_h for holes depend on the local composition and strain, and their computation is discussed in the next subsections. In general, the effective masses and the dielectric constant should also depend on the material and strain fields, but we approximate these as material independent. In principle, the position-dependent effective mass could be included in our calculations, but we have avoided this for simplicity while developing other features. In Sec. 3.3. we discuss extensions to anisotropic effective masses, and in Sec. 3.2. we describe how to include an external magnetic field.

2.1. Atomistic modeling of structures and strain fields

Since path-integral algorithms can directly sample quantum states for any confinement potential, we have taken extra efforts to get realistic input potentials. The effective confining potential for electrons and holes in quantum dots arises from both the local chemical composition and the local strain. Strain significantly changes the confinement, and the 7% lattice mismatch between InAs and GaAs forces us to calculate the strain fields for each structure we consider.

Our starting point is a model for the size, shape, and composition of the nanostructure. Buried InGaAs dots are often represented as a truncated cone or a lens shape (the cleaved top of a sphere). The wetting layer is modeled as a quantum well below the dot. A typical dot contains about 10,000

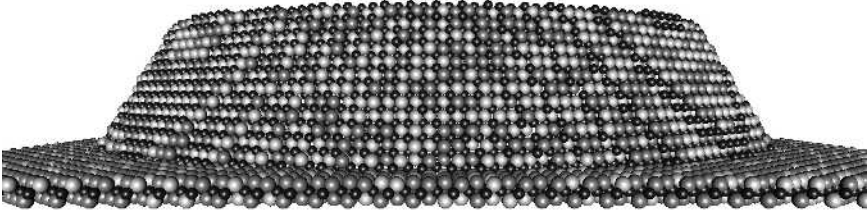


Fig. 1. Image of some of the atoms defining the surface of a conical $\text{In}_{0.6}\text{Ga}_{0.4}\text{As}$ quantum dot model, showing random alloy structure in the dot and wetting layer. This nanostructure is embedded in a bulk GaAs matrix (not shown).

atoms, as shown in Fig. 1. The structure is coherently embedded in the surrounding GaAs matrix. The bulk material around the dot in the model must be thick enough to allow accurate representation of the strain relaxation. Our typical super cell (the nanostructure plus embedding matrix) is approximately 40 nm cubed and contains about 4 million atoms. The compositions of real nanostructures, due to intentional alloying or intermixing of material during the growth process. We can model this by placing atoms in a random alloy structure, and we can even introduce non-uniform composition profiles as suggested by experimental composition measurements.²⁷

To calculate the strain-relaxed structure, we use a valence force field (VFF) model.²⁸ In this model, bond stretching is described with two-atom potential,

$$f_2(r_{ij}) = \frac{3}{8} \alpha_{ij} \frac{(r_{ij} - d_{ij})^2}{d_{ij}^2}, \quad (2)$$

There is also a three-atom interaction to describe bond bending,

$$h(r_{ij}, r_{ik}) = \frac{3}{8} \beta_{ijk} \frac{(r_{ij} r_{ik} \cos(\theta_{ijk}) - d_{ij} d_{ik} \cos(\phi_{ijk}))^2}{d_{ij} d_{ik}}, \quad (3)$$

where $\phi = \cos^{-1}(1/3)$ is the equilibrium tetragonal bond angle. The VFF parameters we use for InGaAs are listed in Table 1. We relax the atomic models to their equilibrium positions using conjugate gradients minimization, as implemented in the code `relax`, available online.²³

Alternatively, we could have used continuum models for the structure compositions and strain and solved the equations using finite elements.^{29,30} We have chosen this atomistic approach so that we can directly compare our

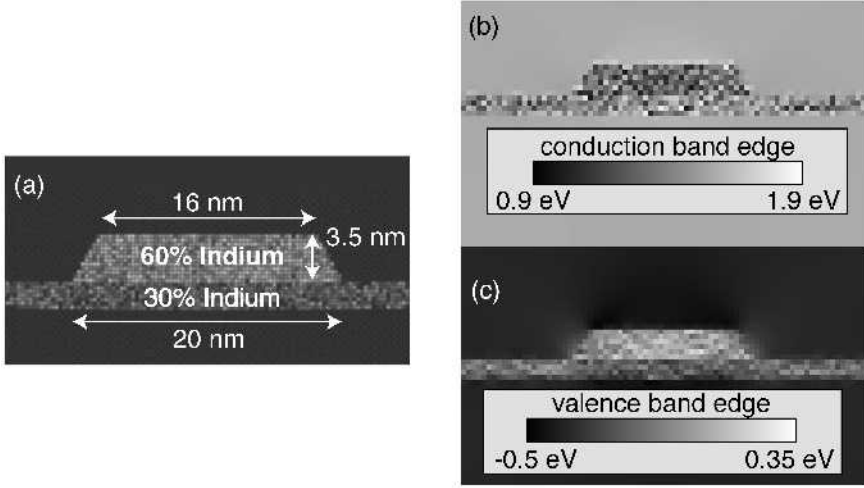


Fig. 2. Extracted single-particle model from structure shown in Fig. 1. (a) The composition, mapped to a cubic grid, and the strain-modified confinement potentials (b) $V_e(\mathbf{r})$ for electrons and (c) $V_h(\mathbf{r})$ for holes.

calculations with empirical pseudopotentials^{27,31} and tight-binding³² models when questions arise about the use of the effective mass approximation.

2.2. Extraction of single-band effective mass models

From the equilibrium atomic positions and residual forces, we calculate local stress tensors at each atom. We then map the stress and composition to a grid, usually with grid spacing of one material lattice constant (so that eight atoms get mapped to one grid point). Using continuum elasticity theory, we map the stress field to a strain field. Finally, we calculate strain and material dependent band offsets. The gridded data for the nanostructure in Fig. 1 are shown in Fig. 2

Table 1. Table of parameters used in our VFF strain model, Eqs. (2) and (3), in atomic units (Ha = 27.211 eV and $a_0=0.529$ Å).

material	α_{ij} (Ha)	$d_{ij}(a_0)$	β_{ijk} (Ha)	$\cos(\phi_{ijk})$
GaAs	0.026311	4.62595	0.0061122	-0.33333
InAs	0.022454	4.97625	0.0039129	-0.33333
InGaAs	—	—	0.0050125	-0.35021

3. PATH INTEGRAL TECHNIQUES FOR DOTS

The thermal density matrix is equal to an imaginary time path integral,^{14,15}

$$\rho(\mathbf{R}, \mathbf{R}'; \beta) \equiv \langle \mathbf{R} | e^{-\beta \hat{H}} | \mathbf{R}' \rangle = \int_{\substack{\mathbf{R}(0)=\mathbf{R}' \\ \mathbf{R}(\beta)=\mathbf{R}}} \mathcal{D}\mathbf{R}(t) \exp \left(-\frac{1}{\hbar} S_E^\beta[\mathbf{R}(t)] \right). \quad (4)$$

where $R = (\mathbf{r}_1, \mathbf{r}_2, \dots, \mathbf{r}_N)$ represent the $3N$ coordinates of the particles. The action $S_E^\beta[\mathbf{R}(t)]$ is the Euclidean, or imaginary-time, action,

$$S_E^\beta[\mathbf{R}(t)] = \int_0^\beta \sum_{i=1}^N \frac{1}{2} m_i^* \dot{\mathbf{r}}_i^2 + V(\mathbf{R}) dt, \quad (5)$$

where the quantity in the integrand is the Euclidean Lagrangian, $\mathcal{L}_E = T + V$. The trace of the density matrix is taken by setting $\mathbf{R} = \mathbf{R}'$ (closing the path) and summing over all paths. Thus, statistical quantum mechanics may be formulated as a weighted sum over closed paths.¹⁴ This is quantum mechanics without Schrödinger's equation: a $3N$ -dimensional quantum problem has been mapped onto the classical partition function of a continuous, polymer-like path.

The real power of the imaginary-time path integral, Eq. (4), is that it is directly applicable to interacting quantum many-body systems. While the exact solution to N interacting quantum particles might seem to require determination of a $3N$ -dimensional wavefunction satisfying a $3N$ -dimensional Schrödinger equation, the path integral formula turns the problem into a computationally tractable $3N$ -dimensional path integral.

As described in Ref. [15], much care must be taken in the discretization and sampling of the path integral. We typically choose a timestep of about $\tau = 4\text{Ha}^{-1}$, so that the particle diffusion is slightly less than one material lattice constant. For low temperature calculations, around $T = 30\text{K} \approx 0.0001\text{Ha}$, this leads to about 2500 slices. We use multilevel Metropolis¹⁵ to sample up to 2^{10} slices in one move. A mixture of levels works best in the sampling: small moves sample details of the confining potential, while large moves help the particles sample regions around the nanostructures. For the gridded potentials, we use a small amount of quantum smoothing in the endpoint (diagonal) approximation.^{14,15} We use a pair approximation¹⁵ to describe the Coulomb interactions over the timestep, τ , using precomputed pair-density-matrix values stored on a grid.

Bose and Fermi statistics enter naturally into the path integral formalism. The partition function for distinguishable particles is simply a sum

over closed paths, $\mathbf{R}(0) = \mathbf{R}(\beta)$. If the particles are indistinguishable, the path integral must be symmetrized or antisymmetrized for Bose and Fermi statistics,

$$\rho_{\text{B/F}}(\mathbf{R}, \mathbf{R}'; \beta) = \sum_P (\pm 1)^P \int_{\substack{\mathbf{R}(0)=\mathbf{R}' \\ \mathbf{R}(\beta)=P\mathbf{R}}} \mathcal{D}\mathbf{R}(t) \exp\left(-\frac{1}{\hbar} S_E^\beta[\mathbf{R}(t)]\right), \quad (6)$$

where P is a permutation of particle coordinates. Thus, the partition function for identical quantum particles includes permuting paths, and these permutations are responsible for Bose and Fermi effects. The minus sign that occurs in the antisymmetrization of fermions is a distinctly quantum feature that generally prevents exact simulations of interacting fermions. Magnetic fields also introduce complex Aharonov-Bohm phases, which cause similar problems. We describe an approximate technique to study fermions in a magnetic field in Sec. 3.2..

Treatment of spin can be a tricky matter. The simplest thing to do is to assign a permanent label of “up” or “down” to each of the particles. The permutations of identical particles are then only allowed between particles with the same spin label. In this formalism, the total component of spin in the z -direction is a constant. At low temperature, when the system occupies a single ground state, this is a reasonable approach, as long as S_z is set to the correct ground state value. For finite temperature, though, a fixed- S_z ensemble is not very physical. There are schemes for sampling the values for S_z during a simulation, but in our current research we are trying a more general approach of keeping the spin degrees of freedom in the path integral. This work is outside the scope of this paper, but we note that the ability of path integral QMC to sample spin excitations and other magnetic effects would be a great benefit to current research in semiconductor nanostructures.

Another issue that comes up with semiconductor nanostructures is band mixing and non-parabolic effective masses. If you identify band indices as an internal degree of freedom, the problem is much like spin. In fact, the six-band Luttinger Hamiltonian³³ for describing valence band mixing resembles the spin-and-isospin-s-dependent Hamiltonians used in nuclear physics. Full treatment of band mixing thus falls outside the scope of this paper. For the simple case of anisotropic effective mass, the real-space QMC methods are directly applicable. We have also developed a method for sampling non-parabolic bands arising from an energy-dependent effective mass,³⁴ which we describe in Sec. 3.3.

3.1. Response of excitonic spectra to electric fields

We are studying the effects of applied electric fields on the photoluminescence spectra of quantum dots. Excitons in these dots are known to have intrinsic dipole moments that couple to electric fields.^{11,35,36} When additional electrons and holes are present in the dot, they act as “spectators” in recombination. Single dot photoluminescence experiments reveal small shifts in exciton recombination energies due to these spectators. We hypothesize that spectators also change the intrinsic dipole moment. By measuring the photoluminescence energies from single dots as a function of applied field, experimentalists should infer some knowledge of the charge distribution in the dots. To make theoretical predictions, we have constructed model quantum dots, Figure 1 and 2, and are running path integral simulations. Preliminary results indicate the effects of spectators are significant and should be measurable in experiments.

The charged nature of the carriers and different confinement properties of electrons and holes are behind two important experiments (1) the study of the linear and non-linear Stark shifts observed in dots in an applied external field^{11,35,36} and (2) the small shifts in exciton energies due to “spectator” electrons and holes observed in single-dot PL experiments.^{5,37,38} In the first of these, the Stark shifts in PL spectra have been attributed to an intrinsic dipole moment due to different confinement properties of electrons and holes, which is then modified by an induced dipole moment from the applied electric field. There has been controversy over the magnitude, and even the sign, of the intrinsic dipole moment, due in part to the strong role of sample-dependent composition profiles in determining the intrinsic dipole moment. In the single-dot PL experiments, subtle interplay direct, exchange, and correlation interactions among the electrons and holes give rise to a rich spectra for even a single quantum dot.

From path integral simulations on our model dot, we have calculated the spectator shift listed in Table 2. There are no discernible blue-shifts in

Table 2. Spectator shifts in a 20 nm truncated cone-shaped $\text{In}_{0.6}\text{Ga}_{0.4}\text{As}$ quantum dot. These are photoluminescence energies and net dipole moments for a bare exciton, charged trions, and a biexciton in an InGaAs quantum dot.

	ΔE (eV)	Δp_z ($e \cdot \text{\AA}$)
X	1.2862(3)	0.06(1)
X ⁻	1.2837(4)	0.30(1)
X ⁺	1.2860(5)	-0.26(1)
XX	1.2849(7)	0.03(1)

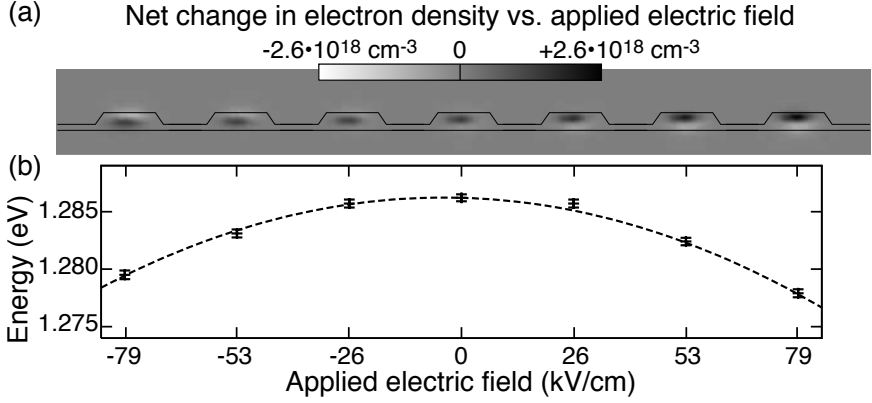


Fig. 3. (a) The distribution of charge density of an exciton in a quantum dot, for seven different values of electric field. An electric field applied in the $+z$ growth direction pushes the electron down (bright, negative charge) and the hole up (dark, positive charge). (b) The corresponding photoluminescence energy spectrum, showing the Stark effect.

energy for any of the spectator states. The negatively charged trion, X^- , shows a clear redshift of about 2 meV. The biexciton is also redshifted, but the magnitude of the shift, ~ 1 meV, is comparable to the statistical error in these Monte Carlo simulations. In the Table, we also list the net dipole moment for the excitonic recombination. We see small intrinsic dipole moments for all states. More pronounced is the dipole moment for recombination from trion states. These dipole moments even differ in sign, which can be understood by if the extra charge moves towards the wetting layer at the base of the dot. After exciton recombination, the remaining spectator charge sits more towards the center of the dot, resulting in the small dipole shift we calculate.

In an electric field, a larger dipole moment can be induced in the dots. We show the distribution of excitonic charge in the seven panels in Fig. 3. Since the path integral samples the density matrix, we can collect the charge distribution functions directly from the simulations. We have applied an external field by placing a small gradient in the potential over the dot. Care must be taken to avoid extremely low potential regions far from the dot, which would lead to ionization of the dot in the thermal simulations. By limiting the electric field to a small region directly around the dot, we have maintained thermodynamically stable simulations for applied fields up to 80

kV/cm. In Fig. 3 the shift in the charge distribution as the applied field is varied is clearly visible. Calculations on excitons, trions, and biexcitons in dots with a variety of composition profiles and external fields are reported in Ref. [39].

3.2. Response to magnetic fields

The electronic and excitonic states in a quantum dot have interesting magnetic field response. Even for single particles, magnetic fields are useful probes for deciphering quantum dot energy spectra, since the magnetic field dependence hints at the angular momentum and lateral extent of the confined states. For multiple particles, the localization of electron states into Landau levels lead to a profound enhancement of coulomb correlation, seen most vividly in the quantum Hall Effect.

The single particle states of a two-dimensional harmonic oscillator in a magnetic field were solved analytically by Fock⁴⁰ and Darwin⁴¹ more than seventy years ago. Experimentally, Ashoori *et al.*¹² observed the Fock-Darwin states using single-electron capacitance spectroscopy. Computer simulations have used exact diagonalization for quantum-dot lithium with strong interaction⁴² and for a four-electron quantum dot⁴³. Density functional theory⁴⁴ and QMC¹⁸ have also been used for such studies.

Quantum simulation of interacting particles is complicated by magnetic fields. The fields introduce a geometric phase into the problem, that remains even in the imaginary-time formulation. Ortiz *et al* have developed a fixed-phase approximation⁴⁵ (later developed independently by Bolton *et al*¹⁸) for ground state QMC simulations in a magnetic field. We have developed a fixed-phase approximation for density matrices suitable for a variety of quantum Monte Carlo algorithms. The derivation uses the maximum entropy principle to map the approximated density matrix to a bosonic problem. As in the wavefunction formulation, the fixed-node approximation is the limiting case for a real-valued trial function. The derivation and discussion of this method can be found in Ref. 46.

This approximation has several advantages over the finite temperature formulation used by Ceperley.⁴⁷ The most significant difference is that our method does not define a “reference slice” as a special time along the path. Some of the advantages of this formalism are: (1) we have a variational proof that this formalism minimizes the free energy, (2) the method is bilocal in imaginary time, allowing efficient imaginary time parallelization, (3) the lack of a reference slice means allows the algorithm to remain efficient as the temperature drops below the Fermi temperature, (4) the formalism naturally

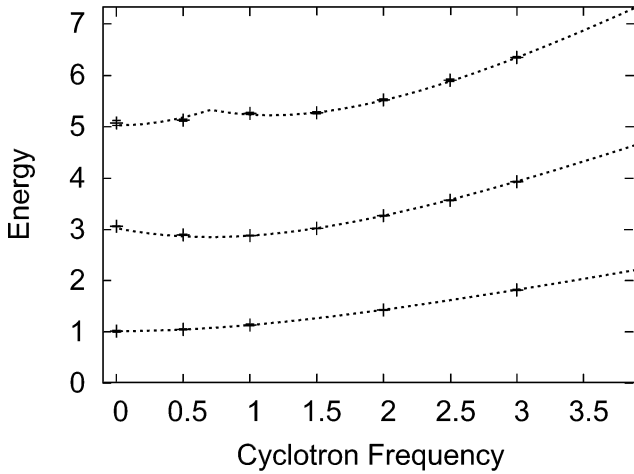


Fig. 4. Preliminary tests for 1–3 fermions in two-dimensional parabolic dot in a magnetic field, as calculated with fixed-phase path integral QMC. Solid lines are analytic results for Fermi filling of the the lowest energy Fock-Darwin states.

includes a fixed-phase approximation, and (5) this general algorithm can also be extended to $T = 0$ simulations for systems with degenerate ground states.

We have tested our fixed-phase path integral algorithm for free fermions in a simple harmonic oscillator potential with a magnetic field, Fig. 4. At low temperature, $k_B T / \hbar \omega = 0.1$, there is excellent agreement with ground state Fock-Darwin energies (solid lines). These tests show that we can efficiently treat both shell filling and magnetic fields with fixed-phase restrictions, thus avoiding the sign (and phase) problems. We are now working on tests with interacting electrons and finite temperature.

3.3. Treatment of non-parabolic conduction bands

A serious limitation of most quantum Monte Carlo simulations on semiconductor nanostructures is the restriction to single-band, parabolic effective mass models. We recently have extended that path integral quantum Monte Carlo technique to treat non-parabolic bands.³⁴ A simple technique for introducing non-parabolicity is to make the effective mass energy dependent, $m^*(\epsilon) = (1 + \alpha\epsilon)m^*(0)$. From $k \cdot p$ theory, the non-parabolicity parameter is the inverse of the band gap. The corresponding energy dispersion

relationship is

$$\varepsilon(k) = \frac{1}{2\alpha} \sqrt{1 + \frac{2\alpha\hbar^2 k^2}{m_0^*}} - \frac{1}{2\alpha}. \quad (7)$$

This is a hyperbola, and is mathematically analogous to relativistic kinetic energy. Essentially, the linear correction to the energy dependent effective mass is equivalent to fitting the conduction band edge to a hyperbola, rather than a parabola. The corresponding propagator is³⁴,

$$G(\mathbf{r}, \mathbf{r}'; \tau) = \frac{\exp\left(\frac{\tau}{2\alpha}\right) \tau}{32\pi^2 \alpha z} \left(\frac{2m_0^*}{\hbar^2 \alpha}\right)^{\frac{3}{2}} K_2(z), \quad (8)$$

where K_2 is a modified Bessel function of the second kind⁴⁸ and

$$z = \frac{\tau}{2\alpha} \left(1 + \frac{2m_0^* \alpha |\mathbf{r} - \mathbf{r}'|^2}{\hbar^2 \tau^2}\right)^{\frac{1}{2}}. \quad (9)$$

For typical times steps in PIMC simulations of dots, the parabolic and non-parabolic actions are different, Fig. 5. Propagation for very short steps and very long steps is enhanced. One consequence is that the midpoint of an imaginary time interval no longer favors the mid-point of the spatial endpoints. The nonparabolic action causes the paths to be non-Brownian at short times: the path tends to stay in one area for a while, then makes a big jump to another location. For longer times Brownian motion is recovered (corresponding to parabolic effective mass), but if the details of the confining potential are small enough to be resolved at shorter times, the effects of band non-parabolicity naturally enter the simulation. Details on the use of non-parabolic effective mass action and tests for an InGaAs dot model can be found in Ref. [34].

3.4. Excitonic recombination rates

The rates of PL processes play a large role in determining the steady-state occupations under continuous photo-excitation of the dot, and can be measured directly in time-resolved experiments.⁷ Essentially, two factors determine the rate: first the recombining electron and hole must be nearby, and second, the material's dipole moment for recombination (given by the Kane parameter⁴⁹) determines the overall recombination rate through Fermi's golden rule. The degree of electron and hole overlap is a property of the few-body states in the nanostructure, and may be estimated from effective mass calculations.

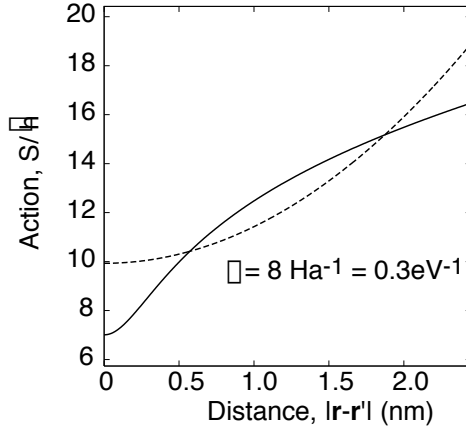


Fig. 5. Comparison of the action for parabolic (dashed line) and non-parabolic (solid line) propagators for a timestep typical for PIMC simulations, $\tau = 8 \text{ Ha}^{-1}$. From Ref. [34].

The role of correlation and spectators in recombination rates has been raised in some recent experiments.^{6,7,50} One simple issue is how the rate of biexciton recombination, Γ_{XX} , relates to the rate of exciton recombination, Γ_X . If interactions are unimportant, as expected for small, strongly confined dots, one expects $\Gamma_{XX}/\Gamma_X \approx 2$, since there are two channels for recombination in the biexciton. On the other hand, correlation is known to suppress recombination in the biexciton, so that a small biexciton trapped in a large quantum dot should have $\Gamma_{XX}/\Gamma_X \approx 1$. Experimental measurements tend to lie throughout that range, with Santori *et al* attributing a measured relative rate of $\Gamma_{XX}/\Gamma_X \approx 1.5$ to significant correlation in the biexciton wavefunction in an InGaAs/GaAs quantum dot.⁷

PIMC can address this problem, as described in detail in Wimmer *et al*.⁵¹ We have calculated the recombination rates of excitons and biexcitons in self-assembled quantum dots,⁵¹ as shown in Fig. 6. By casting the contact matrix element as a path integral, the rate can be determined by a path integral simulation with two boundary conditions, “radiating” and “diagonal,” Fig. 6(a). Denoting the relative contribution of each of these boundary conditions in a Metropolis simulation as $x_{\text{radiating}}$ and x_{diag} , the recombination rate is⁵¹

$$\Gamma_N(\beta) = \frac{2nE_{\text{gap}}E_{\text{Kane}}e^2}{3c^3m} \frac{x_{\text{rad}}}{x_{\text{diag}}}. \quad (10)$$

Fig. 6 shows the PIMC result for Γ_{XX}/Γ_X for an InGaAs/GaAs as a function of dot radius.⁵¹ The important finding was that correlation in the biex-

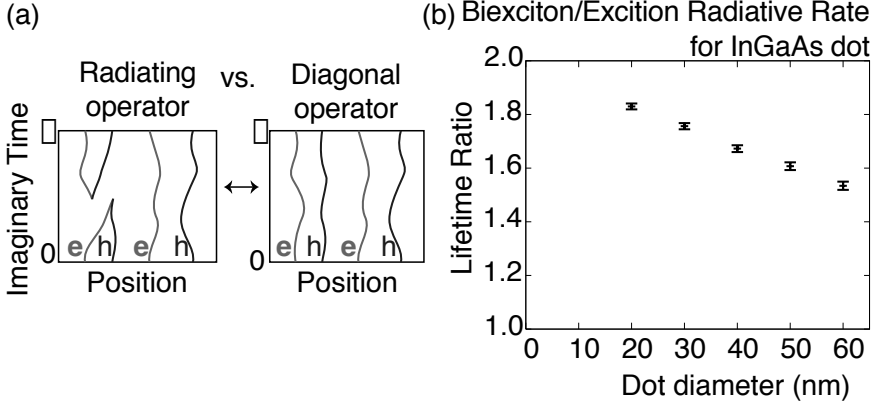


Fig. 6. (a) Recombination rates can be calculated by sampling different boundary conditions on the path integral.⁵¹ (b) PIMC simulation data from Wimmer *et al*,⁵¹, showing the decay rate of a biexciton relative to the exciton rate for InGaAs/GaAs dots with different radii.

citon, which increases for larger dot diameters, does in fact decrease the radiative recombination rate. This is in rough agreement with experimental value⁷ of $\Gamma_{XX}/\Gamma_X \approx 1.5$. Another use of these calculations was to have direct comparison with a competing technique, configuration interaction (CI) multi-determinant expansions.⁵² We have conducted careful tests to verify that the disagreement with CI can be attributed to under-convergence of the CI basis, revealing a strength of our path integral approach.⁵¹

4. CONCLUSION

We have described several recent applications of path integral QMC to the study of self assembled quantum dots. There is a great synergy between the path integral QMC techniques and problems in semiconductor nanostructures. The similar energy scales for quantum confinement, coulomb interaction, and thermal excitations in these nanostructures are helpful for developing and testing new path integral algorithms. Conversely, the ability of path integral QMC to simulate quantum and thermal effects for realistic three-dimensional geometries, external electric and magnetic fields, and material specific effective mass hamiltonians is a great asset to quantum dot theory. Other related structures that could be studied include quantum wells, quantum wires, and quantum point contacts. Also, path-integral QMC and ground state QMC have been used for bulk exciton scattering⁵³

and Bose condensation of excitons.⁵⁴ The extension of these techniques to study excitons in quantum wells or large quantum dots is a natural direction for future study.

It appears that the biggest technical challenges to path integrals is the reliable simulation of finite temperature Fermi systems and the sampling of spin states. With the current scientific and technological interest in magnetic semiconductors and spintronics, the development of path integral QMC as a tool for studying spin effects in warm fermi gases could have a big theoretical impact.

ACKNOWLEDGMENTS

This work supported by the National Science Foundation under Grant No. DMR 0239819.

REFERENCES

1. P. M. Petroff and S. P. DenBaars, *Superlattices and Microstructures* **15**, 15 (1994).
2. L. Jacak, A. Wójs, and P. Harylack, *Quantum Dots*, Springer-Verlag, Berlin, 1998.
3. P. Hawrylak and D. Pfannkuche, *Phys. Rev. Lett.* **70**, 485 (1993).
4. A. Wójs, P. Hawrylak, S. Fafard, and L. Jacak, *Phys. Rev. B* **54**, 5604 (1996).
5. E. Dekel, D. Gershoni, E. Ehrenfreund, J. Garcia, and P. Petroff, *Phys. Rev. B* **61**, 11009 (2000).
6. R. M. Thompson et al., *Phys. Rev. B* **64**, 201302 (2001).
7. C. Santori, G. S. Solomon, M. Pelton, and Y. Yamamoto, *Phys. Rev. B* **65**, 073310 (2002).
8. M. Bayer et al., *Science* **291**, 451 (2001).
9. G. Bester, J. Shumway, and A. Zunger, *Phys. Rev. Lett.* **93**, 047401 (2004).
10. J. Shumway, A. Franceschetti, and A. Zunger, *Phys. Rev. B* **63**, 155316 (2001).
11. S. Raymond et al., *Phys. Rev. B* **58**, R13415 (1998).
12. R. C. Ashoori et al., *Phys. Rev. Lett.* **71**, 613 (1993).
13. S. Raymond et al., *Solid State Comm.* **101**, 883 (1997).
14. R. P. Feynman, *Statistical Mechanics*, Addison-Wesley, Reading, MA, 1972.
15. D. M. Ceperley, *Rev. Mod. Phys.* **67**, 279 (1995).
16. Y. Z. Hu et al., *Phys. Rev. Lett.* **64**, 1805 (1990).
17. E. L. Pollock and S. W. Koch, *J. Chem. Phys.* **94**, 6776 (1991).
18. F. Bolton, *Phys. Rev. B* **54**, 4780 (1996).
19. E. Lee, A. Puzder, M. Y. Chou, T. Uzer, and D. Farrelly, *Phys. Rev. B* **57**, 12281 (1998).
20. J. Shumway, L. R. C. Fonseca, J. P. Leburton, R. M. Martin, and D. M. Ceperley, *Physica E* **8**, 260 (2000).

21. F. Luczak, F. Brosens, J. T. Devreese, and L. F. Lemmens, *Phys. Stat. Sol. (b)* **225**, 413 (2001).
22. J. Harting, O. Mülken, , and P. Borrmann, *Phys. Rev. B* **62**, 10207 (2000).
23. Open-source codes, documentation, and other information are available online at <http://physics.asu.edu/shumway/codes/>.
24. I. N. Stranski and V. L. Krastanow, *Akad. Wiss. Lit. Mainz Math.-Natur. Kl. IIb* **146**, 797 (1939).
25. D. J. Eaglesham and M. Cerullo, *Phys. Rev. Lett.* **64**, 1943 (1990).
26. O. Brandt et al., *Phys. Rev. B* **45**, 8443 (1992).
27. J. Shumway et al., *Phys. Rev. B* **64**, 125302 (2001).
28. P. N. Keating, *Phys. Rev* **145**, 637 (1966).
29. M. Grundmann, O. Stier, and D. Bimberg, *Phys. Rev. B* **52**, 11969 (1995).
30. L. R. C. Fonseca, J. L. Jimenez, J. P. Leburton, and R. M. Martin, *Phys. Rev. B* **57**, 4017 (1998).
31. A. J. Williamson and A. Zunger, *Phys. Rev. B* **61**, 1978 (2000).
32. S. Lee, L. Jönsson, J. W. Wilkins, G. W. Bryant, and G. Klimeck, *Phys. Rev. B* **63**, 235307 (2002).
33. J. M. Luttinger, *Phys. Rev* **102**, 1030 (1956).
34. J. Shumway, "A quantum Monte Carlo method for non-parabolic electron bands in semiconductor heterostructures," submitted to *J. Phys.: Condens. Matter*, 2005.
35. P. W. Fry et al., *Phys. Rev. Lett.* **84**, 733 (2000).
36. P. W. Fry et al., *Phys. Rev. B* **62**, 16784 (2000).
37. E. Dekel et al., *Phys. Rev. Lett.* **80**, 4991 (1998).
38. A. Zrenner, *J. Chem. Phys.* **112**, 7790 (2000).
39. M. Harowitz and J. Shumway, "Stark shifts of excitons and biexcitons in quantum dots," in preparation for submission to *Phys. Rev. B*, 2005.
40. V. Fock, *Z. Phy.* **47**, 446 (1928).
41. D. G. Darwin, *Proc. Cambridge Philos. Soc.* **27**, 86 (1930).
42. S. A. Mikhailov and N. A. Savostianova, *Phys. Rev. B* **66**, 033307 (2002).
43. M. B. Tavernier et al., *Phys. Rev. B* **68**, 205305:1 (2003).
44. M. Ferconi and G. Vignale, *Phys. Rev. B* **50**, 14722 (1994).
45. G. Ortiz, D. M. Ceperley, and R. M. Martin, *Phys. Rev. Lett.* **71**, 2777 (1993).
46. D. Shin and J. Shumway, "Density-matrix-based fixed-phase approximation for quantum Monte Carlo simulations," in preparation, 2005.
47. D. M. Ceperley, *Phys. Rev. Lett.* **69**, 331 (1992).
48. M. Abramowitz and I. Stegun, *Handbook of Mathematical Functions*, Dover Publications, Inc., New York, 1970.
49. E. O. Kane, *J. Phys. Chem. Solids* **1**, 249 (1957).
50. G. Bacher et al., *Phys. Rev. Lett.* **83**, 4417 (1999).
51. M. Wimmer, J. Shumway, and S. V. Nair, (2005), in preparation for submission to *Phys. Rev. B*.
52. S. Corni, M. Braskén, M. Lindberg, J. Olsen, and D. Sundholm, *Phys. Rev. B* **67**, 045313 (2003).
53. J. Shumway and D. M. Ceperley, *Phys. Rev. B* **63**, 165209 (2001).
54. J. Shumway and D. M. Ceperley, *Solid State Comm.* **134**, 19 (2005).